Plasma-Devised Pt/C Model Electrodes for Understanding Doubly Beneficial Roles of Nanoneedle-Carbon Morphology and Strong Pt-Carbon Interface in Oxygen Reduction Reaction

Xiao Zhao[a], Yutaka Hamamura[b], Yusuke Yoshida[a], Takuma Kaneko[a], Takao Gunji[a], Shinobu Takao[a], Kotaro Higashi[a], Tomoya Uruga[a,c], and Yasuhiro Iwasawa[a,d*]

[a] Innovation Research Center for Fuel Cells, The University of Electro-Communications, Chofu, Tokyo 182-8585, Japan

[b] Materials & Advanced Research Laboratory, Nikon Corporation Sagamihara, kanagawa 252-0328, Japan

[c] Japan Synchrotron Radiation Research Institute, SPring-8 Sayo, Hyogo 679-5198, Japan

[d] Department of Engineering Science, Graduate School of Informatics and Engineering, The University of Electro-Communications, Chofu, Tokyo 182-8585, Japan

Keywords. Nanoneedle-carbon morphology effect, Plasma-fabricated strong Pt-carbon interface, Devised Pt/C model electrode, Oxygen reduction reaction, Electrocatalytic activity and durability.

ABSTRACT: The doubly beneficial contribution of nanoscale fabricated carbon surface and devised strong Pt-carbon interface to remarkable improvements of Pt/carbon fuel cell electrodes was evidenced to be a crucial clue for rational design of next-generation less-Pt/C electrodes. Real-world carbon surface morphology and metal-carbon interface are complex and interrelated, which are hard to control at a statistical level. Herein, we fabricated plasma-devised nanoneedles-glassy carbon (GC) from well-defined flat GC as model supports, on which Pt nanoparticles were anchored by arc plasma. The arc plasma deposited (APD)-Pt/flat-GC with strong metal-support interface exhibited enhanced activity for electrochemical oxygen reduction reaction (ORR) compared to chemically supported Pt/flat-GC and commercial Pt/C electrodes. The APD-Pt/nanoneedles-GC further promoted the ORR and showed a remarkable durability without significant deactivation after accelerated durability test cycles. The structural defects and compressive strain of Pt nanoparticles were induced by the plasma-devised metal-support contact, which may benefit the ORR activity of APD-Pt/nanoneedles-GC. The nanoneedles-GC support morphology may also improve oxygen gas transport at nanoscale through modifying the hydrophobicity/hydrophilicity of the GC surface. These results on the devised Pt/C model electrodes reveal the highly enhanced activity and durability of the APD-Pt/nanoneedles-GC electrode by the doubly beneficial effects of support nanoscale morphology and strong metal–support interface, which were characterized by the intimate combination of the Pt/GC synthesis, electrochemical measurements, *in situ* XAFS and HAADF-STEM. Our experimental findings provide necessary clues for the design and synthesis of active and durable fuel cell electrodes, metal-air batteries, and catalytic materials.

1. INTRODUCTION

Supported precious metals are widely used as catalysts for a range of fundamental and industrially important reactions; e.g. Pt/C electrocatalyzes oxygen reduction reaction (ORR) in fuel cells. However, high cost and scarcity of precious metal catalysts need new clues to improve their activity and durability remarkably.[1-3] Pt alloying with other metals such as Fe, Co, and Ni brings about ligand and geometric effects, resulting in improved catalytic properties due to modified Pt electronic structure and binding energy with reaction intermediates. The control of Pt shapes, facets and lattice strains is an alternative strategy. Recently, high-curvature nanoneedle-like catalysts have received intensive attention in electrocatalysis. The high-index facets and undercoordinated sites around tips induce an intrinsic change in electronic structures.[4] The facet surfaces also regulate mass transport[5] and induce a local high electric field, which improves adsorbate concentrations.[6-9] However, these coexisting structural impacts are interrelated with each other, which makes their discrimination and understanding quite difficult. This dilemma also happens with most of heterogeneous metal catalysts and few feasible methods are proposed to find out these interrelated structural effects on the origin and genesis of supported metal catalysis.

Supports for Pt electrocatalysts, especially in membrane electrode assembly (MEA) in polymer electrolyte fuel cell (PEFC) affect ORR performance profoundly from multi-prospects through metal-support contact, interfacial sites, hydrophilicity/ hydrophobicity, surface area, porosity, etc. and provide conductive paths and mass-transport frameworks.[10-13] Real-world supports are structurally complex due to many factors, such as surface doping, chemically functional groups, support curvature, defects, etc., which are usually hard to control at a statistical level. Under these conditions, the fine understanding of the doubly beneficial effects of support nanoscale morphology and strong metal-support interface based on controlled surface fabrication and high-energy metal deposition is essentially challenging due to their multiple interrelated structural factors. Due to the instability of carbon black in fuel cell operations,

alternative carbon supports for ORR have been developed; e.g. electrospun carbon nanofiber,[14] multiwalled carbon nanotubes (MWCNTs), reduced graphene oxide (rGO) and a nanocomposite of indium tin oxide with rGO,[15] where MWCNTs showed the smallest degradation.

Herein, we used a well-defined flat glassy carbon (GC) disk as a model support, on which Pt nanoparticles were anchored by an arc plasma deposition (APD) method. We also fabricated plasma-devised nanoneedle arrays on the flat GC surface layers and subsequently Pt nanoparticles were anchored on the nanoneedles-GC by the APD technique. For comparison, chemically supported Pt on flat-GC was also prepared, where at first Pt nanoparticles were synthesized by ethylene glycol reduction of chloroplatinic acid precursor and then deposited on the flat GC disk by drop casting. Doubly beneficial effects of the novel support nanoscale morphology and strong Pt–GC support interface at a statistical level on ORR activity and durability were studied by the intimate combination of controlled fabrications of model electrodes, electrochemical measurements under well-defined mass transport conditions, *in situ* X-ray absorption fine structures (XAFS), and high-angle annular dark-field scanning transmission electron microscopy (HAADF-STEM). More specifically, the APD-Pt/nanoneedles-GC electrode with the support nanoscale morphology and high-energy Pt–carbon contact exhibited a negligible loss of the ORR activity (no loss of mass activity (MA)) after 10,000 potential-load (0.6–1.0 V) cycles compared to 42.5% MA loss for the chemically supported Pt/flat-GC and 25% MA loss for a benchmark Pt/C (TEC10E50E-HT), while promoting the ORR activity (MA) by a factor of 4.5 or 6.3 compared to the chemically supported Pt/flat-GC and Pt/C, respectively. The fundamental information on the devised Pt/C model electrodes provides new approach and prospect for conceiving and fabricating active and durable fuel cell electrodes, metal-air batteries, and catalytic materials.

2. EXPERIMENTAL SECTION

2.1. Fabrications of nanoneedles on GC. Nanoneedles on flat glassy carbon (GC) disk surface were produced by using an inductively coupled plasma (ICP)-reactive ion etching (RIE) system (RIE-101iPH Samco Inc.). A flat GC disk with a diameter of 5 mm (Purchased from Pine Research Instrumentation) was placed on an alumina tray. The optimized recipe for dry etch of the flat GC surface is as follows; a mixture gas: O_2 of 14 sccm (standard cubic centimeters per minute), CHF_3 of 14 sccm, and Ar of 14 sccm; gas pressure: 7 Pa; ICP power: 500 W; radio frequency (RF) power: 100 W; etching time: 30 s. After the plasma-etching, the samples were washed by a 10% HF solution for 60 s and then pure water for 3 min, and finally dried at room temperature. Recently, plasma physics for fabrications of nanocarbons such as nanotubes, carbon nanohorns, graphene, carbon nanowalls, carbon nanobelt, etc. has been reviewed though it is entirely different from our plasma-devised surface fabrication technique.[16]

2.2. Arc plasma depositions of Pt nanoparticles on the flat-GC and nanoneedles-GC (denoted as APD-Pt/flat-GC and APD-Pt/nanoneedles-GC). The deposition of Pt nanoparticles on the flat-GC or nanoneedles-GC was conducted at a discharge voltage of 70 V with the capacitance of capacitor 360 μF at 3 Hz in an arc plasma deposition system (ADVANCE RIKO, Inc). The Pt amounts deposited on the GC surfaces were estimated from the calibration curve for the Pt amount deposited on a Si wafer (500 μm thick) substrate vs. the number of APD shots using a film thickness meter (Bruker, DektakXT). The Pt deposited amount (μg cm^{-2}) can be calculated from the equation, Pt film thickness (μm $x10^{-4}$) x Pt density (21.45 g cm^{-3}) x 10^{-6}. For comparison, Pt deposition was performed at the capacitance of capacitor 50 μF at a discharge voltage of 70 V, but no Pt deposition occurred, which suggests a threshold power for arc plasma deposition of Pt on glassy carbon. In this study the above Pt deposition condition was fixed to study doubly beneficial roles of nanoneedle-carbon morphology and strong Pt-carbon contact in ORR. The mass and thus particle density of Pt on the flat-GC and nanoneedles-GC were regulated by the number of APD shots. The deposited Pt amounts for APD-Pt/flat-GC and APD-Pt/nanoneedles-GC used in this study were 2.6 μg Pt/cm^{-2}

and 3.1 μg Pt/cm^{-2}, respectively. Recently, an arc plasma deposition method has been applied for preparation of Pt-Ni thin films on amorphous carbon with different approach and aim from the current unique ones.[17]

2.3. Preparation of chemically supported Pt/flat-GC sample (denoted as chem-Pt/flat-GC). Chemically supported Pt/flat-GC electrode was prepared as follows. 20 mL of ethylene glycol, 0.1 mL of 1.94 M sodium hydroxide aqueous solution and 0.1 mL of 0.077 M chloroplatinic acid aqueous solution were added to a 150 ml pressure vessel. After 15 min stirring and 30 min ultra-sonication mixing, the vessel with the yellow reaction solution was dipped into an oil bath at 180 °C. The color of the reaction solution changed to light black after about 4 min. The vessel was finally taken out from the heating oil bath to end the reaction after 18 min. The 60 mL of 0.1 M perchloric acid solution was added in the above reaction solution to promote the subsequent collection of Pt nanoparticles by centrifugation at 1,5000 rpm for 30 min. The Pt nanoparticles were redispersed in 10 mL ethanol and 10 μL Pt nanoparticles solution was dropped on a flat GC support. After drying, a small amount of Nafion solution (5 μL, 0.03 wt.% Nafion® solutions) at a Nafion ionomer/Pt weight ratio of 0.1) was dropped for fixing Pt NPs on the GC surface. This thin ionomer layer might affect O_2 mass transport, but we optimized the quantity of catalyst thin film to ensure that diffusion-controlled limiting currents are similar between the electrodes examined in this study (about 5.8 mA cm$^{-2}_{geo}$ at 1600 rpm). As such, it is regarded that using the small amount of Nafion does not block the O_2 mass transport significantly and does not change the trend in the ORR activity order for the examined electrodes.

2.4. Electrochemical Measurements. All glassware for electrochemical measurements was treated by aqua regia and then by boiled water and washed by Millipore water thoroughly. A 0.1 M $HClO_4$ solution was prepared using perchloric Acid (TraceSELECT®, Sigma-Aldrich) and 18.2 MΩ·cm Millipore water. As-prepared electrodes were used as the working electrode for electrochemical measurements. The testing temperature was room temperature. Pt foil and RHE were used as counter and

reference electrodes, respectively. The working electrodes were treated by an electrochemical activation process by repeated potential cycles (typically 50 cycles) from 0.02 to 1.2 V (vs RHE) at a scan rate of 100 mV s^{-1} in N_2-saturated 0.1 M $HClO_4$ until a stable response was obtained. Cyclic voltammetry was measured at a scan rate of 50 mV s^{-1} in N_2-saturated 0.1 M $HClO_4$. Electrocatalytic performances for oxygen reduction reaction (ORR) were estimated by linear sweep voltammetry (LSV) from 0.0 to 1.05 V at a scan rate of 20 mV s^{-1} in O_2-saturated 0.1 M $HClO_4$ at 1600 rpm. As the ORR activity measurement at RDE depends on the quality of catalyst thin film, the Pt loading and measurement procedure were optimized to ensure well-defined ORR polarization curves. The ORR performances were calculated by the Koutecky-Levich equation and normalized with Pt mass and ECSA to obtain mass activity (MA) and surface specific activity (SA), respectively. The Tafel analysis shows the consistent trend in the SA. The ORR activity was determined at 0.9 V. The measurements were repeated three times and an averaging value was used for calculations of MS and SA. The solution resistance R_{sol} was measured by the i-interrupter method and used for IR-compensation. Accelerated durability test (ADT) load cycles were conducted by rectangular-wave 0.6–1.0 V potential cycles of 3 s at each of 0.6 and 1.0 V up to 10,000 cycles in O_2-saturated 0.1 M $HClO_4$.

2.5. Preparation of STEM specimen. Firstly, epoxy resin (G2 epoxy: GATAN) was used to protect the electrode surface by the formation of a coating/wrapping layer. After cutting to a given thickness of the wrapping electrode by diamond cutter, the ion slicer (EM-09100IS) was used for thin film processing using Ar ion milling.

2.6. HAADF-STEM images and EDS maps. JEM-ARM200F (JEOL) equipped with a chemical analyzer (JED-2300T DrySDD 100 mm) at an accelerating voltage of 200 kV was used for HAADF-STEM and EDS. The contrast profiles for HAADF-STEM image were obtained using ImageJ software. The error of averaged Pt d(111) lattice spacings is brought about from the error in measuring the size of a Pt nanoparticle.

Cross-sectional high resolution STEM/SEM images were also recorded with cold field emission electron microscope SU9000 (Hitachi) at an accelerating voltage of 10 kV.

2.7. *In situ* X-ray absorption fine structure (XAFS). After the electrochemical measurements the working electrodes were analyzed by *in situ* XAFS. *In situ* XAFS measurements were conducted in N_2-saturated 0.1 M $HClO_4$ in a home-made electrochemical cell at 1600 rpm.[18] The measurements of *in situ* XAFS spectra at Pt L_3-edge were performed in a fluorescence mode by using a Si(111) double-crystal monochromator and an ion chamber (I_0: Ar 5% / N_2 95%) for incident X-rays and a 21 Ge-elements detector for fluorescent X-rays at BL36XU beamline in SPring-8.[19] X-ray absorption near-edge structure (XANES) spectra were normalized by Athena software. The XAFS spectra were treated with the data analysis program IFEFFIT (version 1.2.11c). Theoretical phase shift and amplitude functions for Pt-Pt and Pt-O were calculated from FEFF 8.4 and used for curve fitting processes. The extracted EXAFS (extended X-ray absorption fine structure) oscillations were k^2-weighted and Fourier transformed to R-space. The curve fittings of k^2-weighted EXAFS data in R-space were carried out with Artemis software.[20,21]

3. RESULTS AND DISCUSSION

Figure 1a illustrates the fabrication of arc plasma deposited (APD) Pt nanoparticles (NPs) anchored on plasma-etched nanoneedles-GC (APD-Pt/nanoneedles-GC electrode). Nanoneedles-GC surface was produced by plasma etching of a flat GC in a mixture gas of O_2, CHF_3, and Ar. The resultant nanoneedles were visualized in SEM images (Figure 1 b & c). The estimated heights of nanoneedles were in the range of 50-140 nm (av:108±20 nm) and the section widths of tips of nanoneedles were in the range of 4-13 nm (av: 8±2 nm). Pt NPs were anchored on the nanoneedles-GC by an arc plasma deposition method. Figure 1 d & e show cross-sectional high-resolution (HR) SEM images of two typical APD-Pt/nanoneedles-GC electrodes, where Pt grains are observed

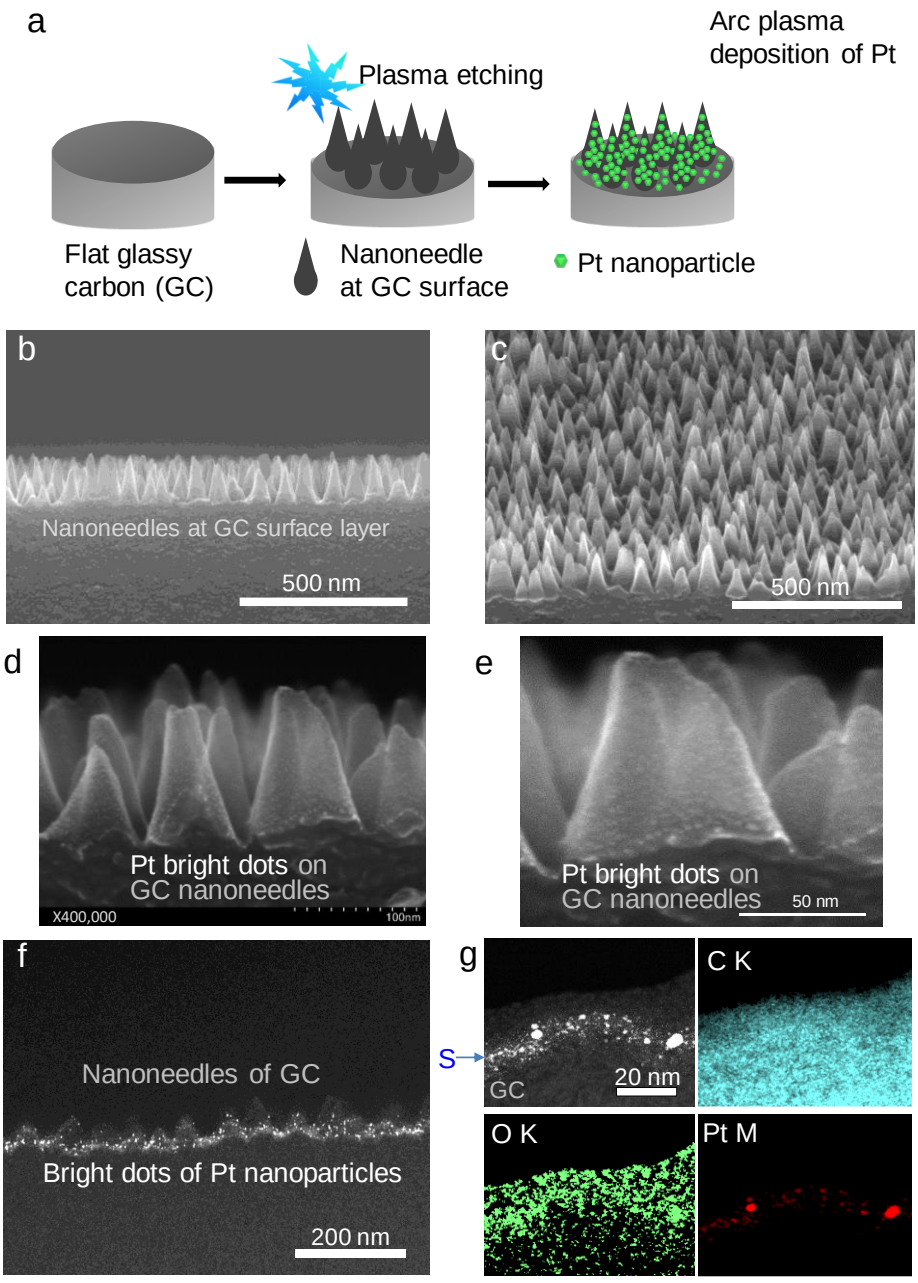

Figure 1. (a) Fabrication steps for the APD-Pt/nanoneedles-GC model electrode. (b, c) Cross-sectional and perspective views of SEM images of etched GC with nanoneedles, respectively. (d) Cross-sectional HR-SEM images of a typical APD-Pt/nanoneedles-GC electrode (x 400,000 magnification). (e) Zoomed image of (d). (f) Cross-sectional HAADF-STEM image of the nanoneedles-GC electrode with Pt nanoparticles as bright dot images. (g) Cross-sectional HAADF-STEM image of a single GC nanoneedle with bright Pt nanoparticle dots (it is not cut via the nanoneedle vertex) and the corresponding C, O, and Pt EDS element maps. Arrow S in (g) indicates the surface of GC support. The HAADF-STEM images were observed after electrochemical measurements.

as thin bright dots on the nanoneedles-GC. Figure 1 f is a representative cross-sectional HAADF-STEM image of the APD-Pt/nanoneedles-GC electrode with Pt NPs as bright dot images. Pt NPs with an average size of 2.3±0.7 nm are distributed on the nanoneedles-GC surface, while part of Pt NPs look to be embedded in the nanoneedles-GC surface layers (Figure 1 f and Figure S1). Figure 1 g shows a typical cross-sectional HAADF-STEM image of a single GC nanoneedle with bright Pt NPs dots (it is not cut via the nanoneedle vertex) and the corresponding Pt EDS element map. Arrow S in Figure 1 g indicates the topmost surface of GC support, which was estimated from the difference in the signal intensity of the O EDS element map between the GC and the covering epoxy resin. The HAADF-STEM images were observed after electrochemical measurements.

We prepared other two model electrodes to explore the effects of GC-support nanoscale morphology and strong Pt–GC interface (Figure 2 a-c & d). For scrutinizing the support nanoscale morphology effect, high-energy Pt by the APD method was deposited, similar to the case of the APD-Pt/nanoneedles-GC electrode, but on a flat GC support instead of the nanoneedles-GC as shown in Figure 2a. Cross-sectional HAADF-STEM images and EDS element maps visualize the feature of APD-Pt/flat-GC (Figure 2b, c) with an average Pt size of 1.8±0.3 nm (Figure S2). In the APD process, Pt ions with high kinetic energies generated by arc plasma collided and subsequently interacted strongly with the GC surface, bringing about strong interaction between Pt NPs and carbon defects. On the other hand, to explore strong metal-support interface and its effect on ORR catalysis, a Pt/flat-GC electrode (chem-Pt/flat-GC) was also prepared by drop-casting of Pt NPs dispersion on the flat-GC and then by using a diluted Nafion® solution to fix drop-casted Pt NPs on the flat-GC support. Pt NPs used for the drop-casting were synthesized by an ethylene glycol reduction method and possessed an averaging particle size of 3.1±0.5 nm (Figure S3).

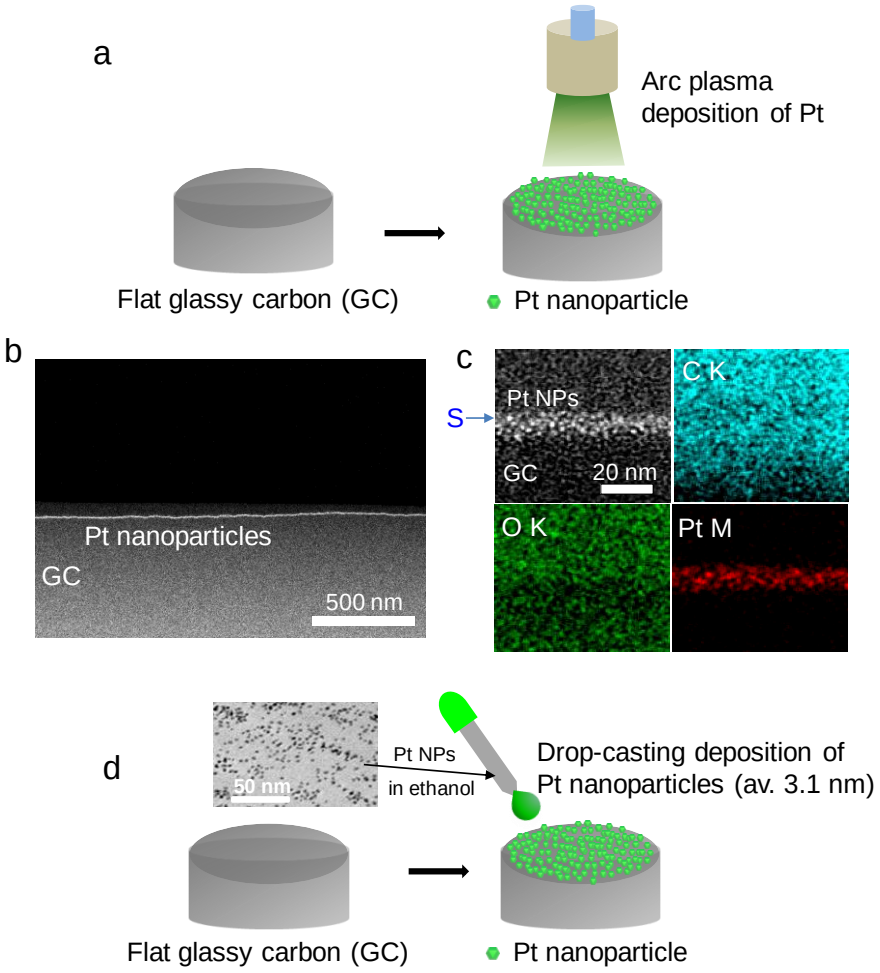

Figure 2. (a) Fabrication steps of APD-Pt/flat-GC model electrode. (b, c) Cross-sectional HAADF-STEM images and EDS element maps of the APD-Pt/flat-GC electrode. (d) Fabrication steps of chem-Pt/flat-GC model electrode. The HAADF-STEM images (b, c) were observed after electrochemical measurements. Arrow S in (c) indicates the surface of GC support.

We selected ORR as a model reaction because of its crucial importance in fuel cell and metal-air battery techniques.[22-24] The electrochemical fingerprints from adsorbed CO (CO_{ad}) stripping voltammetry reveal surface-sensitive structural information. In terms of the upper potential vertex of 1.2 V_{RHE}, Pt surface oxides could be produced, thus the cathodic reduction peak at 0.7–0.8 V_{RHE} may comprise contributions from desorption of both O/OH species and surface oxide.[23,25] However, the reduction peak potential indicates deoxygenation capability of electrocatalysts, i.e. more positive potential suggest easier desorption/reduction of oxygenated species. The cathodic peak potentials

seen from the negative scan of voltammograms (Figure 3a) are in the order of APD-Pt/nanoneedles-GC ≈ APD-Pt/flat-GC > chem-Pt/flat-GC > Pt/C, which suggests the weaker oxygen-binding strength and easier desorption/reduction of O/OH and surface oxides and the down-shifted d-electronic states for the APD-Pt/flat-GC and APD-Pt/nanoneedles-GC electrodes. The electrochemical trend is consistent with the *in situ* XANES, where the suppression of Pt oxidation was observed with the APD-Pt/nanoneedles-GC electrode (discussed later). The CO_{ad} stripping peak potentials in Figure 3a showed the order of APD-Pt/nanoneedles-GC (0.750 V_{RHE}) < APD-Pt/flat-GC (0.832 V_{RHE}) < chem-Pt/flat-GC (0.847 V_{RHE}) ≤ Pt/C (0.841–0.878 V_{RHE}, depending on the kind of commercial samples). The kinetics of CO_{ad} oxidation is determined by the adsorption energy of CO_{ad} and the accessibility to reactive O/OH species that are usually generated on defect sites like steps at low potentials prior to the CO_{ad} stripping oxidation. The easiest oxidation of CO_{ad} on the APD-Pt/nanoneedles-GC among the examined electrodes indicates the weakened strength of CO adsorption and/or the existence of defect sites. The atom-resolved HAADF-STEM images in Figure 4 show existence of low-coordinated step defects on both APD-Pt/nanoneedles-GC and APD-Pt/flat-GC, presumably caused by the APD treatment. The electrochemically active surface areas (ECSA) estimated by the integrated charge of CO_{ad} oxidation were 45, 43, 35 and 48 m^2 g^{-1}_{Pt} for Pt/C, chem-Pt/flat-GC, APD-Pt/flat-GC, and APD-Pt/nanoneedles-GC, respectively. The relatively smaller ECSAs for the APD-Pt/flat-GC and APD-Pt/nanoneedles-GC than those estimated from their averaged particle sizes are due to Pt NPs partially embedded in GC as imaged in Figure 1d-g, Figure S1, Figure 2c, and Figure S2. As the ORR activity measurement by the rotating disc electrode technique depends on the quality of catalyst thin film,[26-28] the Pt loading and the measurement procedure were optimized to ensure well-defined ORR polarization curves (Figure 3b and Figure S4). The ORR mass activity (MA) (Figure 3c) and specific activity (SA) (Figure 3d) were evaluated by the Koutecky-Levich equation on the basis of the ORR polarization curves at a scan rate of 20 mV/s in O_2-saturated 0.1 M $HClO_4$

electrolytes at 1600 rpm (Figure 3b and Figure S4) with the trend: APD-Pt/nanoneedles-GC > APD-Pt/flat-GC > chem-Pt/flat-GC ≥ Pt/C. In Figure 3c & d, the larger MA and SA are observed for both APD-Pt/nanoneedles-GC and APD-Pt/flat-GC compared to the chem-Pt/flat-GC, suggesting strong Pt–GC support interaction-enhanced ORR activities. Further, the surface specific activity (SA) for the APD-Pt/nanoneedles-GC was improved compared to the APD-Pt/flat-GC. Thus, the enhanced ORR activity is contributed by Pt NPs deposited on the nanoneedles-GC, showing a beneficial support nanoscale morphology effect.

Another striking feature of the APD-Pt/nanoneedles-GC is high durability. The APD-Pt/nanoneedles-GC showed negligible MA loss after the accelerated durability test (ADT) of 10,000 cycles between 0.6 and 1.0 V_{RHE} (Figure 3e & f). In contrast, the APD-Pt/flat-GC showed 14.7% MA loss after the 10,000 ADT cycles (Figure 3f and Figure S4), indicating a significant effect of the nanoneedles array on the durability. Further, the chem-Pt/flat-GC revealed the largest loss of MA (-42.5% against the MA before the ADT) among the four electrodes (Figure 3f and Figure S5). The large difference between the chem-Pt/flat-GC and APD-Pt/flat-GC in the MA loss suggests a large influence of the strong metal–support interface generated by the high-energy Pt deposition on the GC on the durability. The degradation paths for Pt/C-based catalysts consist of Pt dissolution, Pt detachment, carbon corrosion, Ostwald ripening, and agglomeration.[29-31] As the result of the strong Pt–GC contact and the robust stability of GC in the APD-Pt/flat-GC and particularly APD-Pt/nanoneedles-GC, the degradation pathways can be released and suppressed greatly. In particular, the electronic and structural regulations of Pt NPs could be realized through the devised Pt/C model electrodes produced by the arc plasma Pt deposition and plasma-fabricated nanoneedles-GC as suggested by HAADF-STEM and *in situ* XAFS below.

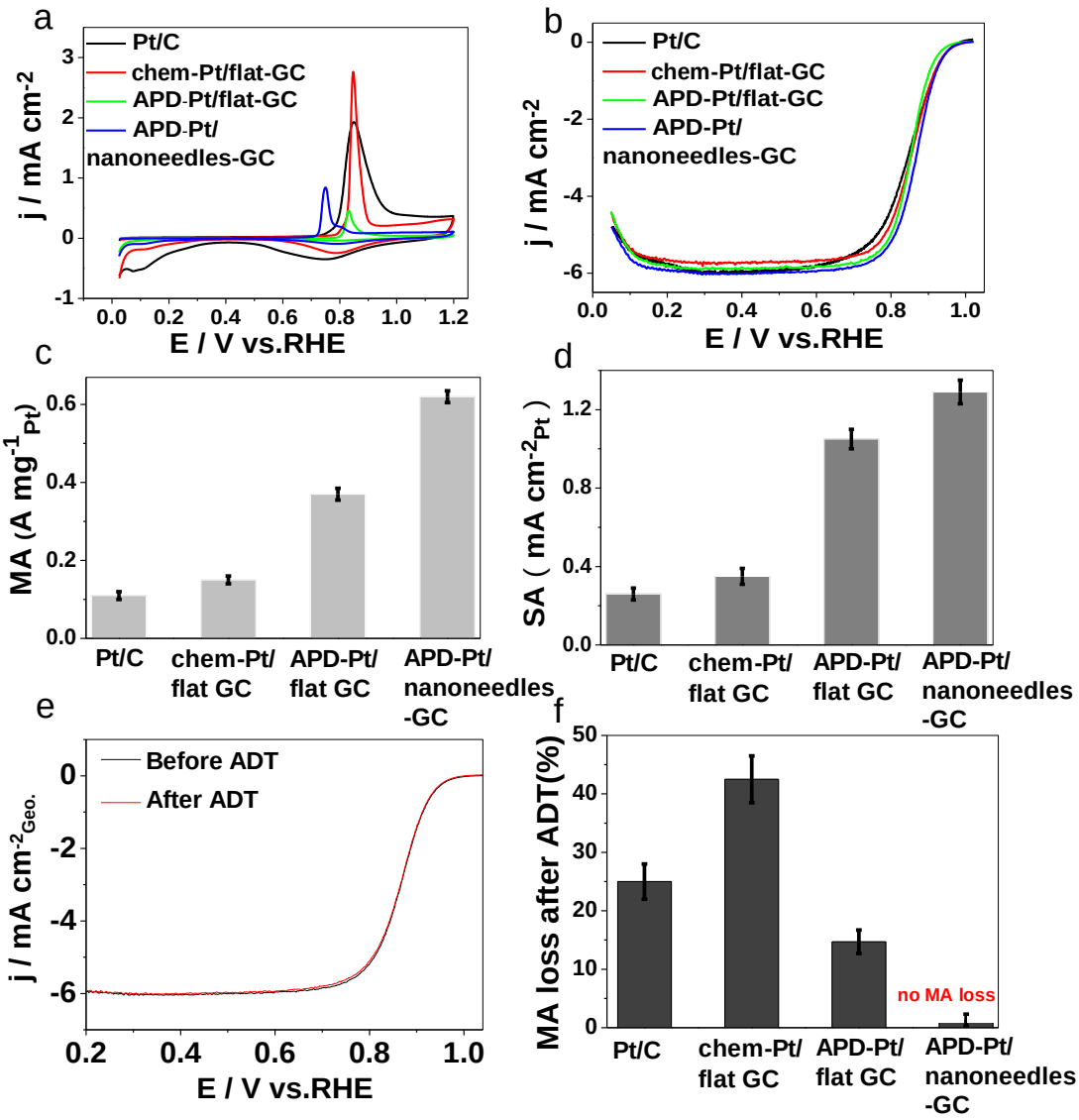

Figure 3. Electrochemical performances of the model electrodes. (a) Adsorbed CO oxidation voltammograms at a scan rate of 50 mV/s. (b) ORR polarization curves at a scan rate of 20 mV/s in O_2-saturated 0.1 M $HClO_4$ aqueous electrolyte at 1600 rpm. (c, d) Histograms for mass activity (MA) and surface specific activity (SA); MA and SA were calculated by the Koutecky-Levich equation. The ORR activity was determined at 0.9 V_{RHE}. (e) ORR polarization curves of APD-Pt/nanoneedles-GC before and after ADT. (f) MA losses of the model electrodes after the ADT. ADT procedure: 10,000 potential cycles between 0.6 and 1.0 V_{RHE} each 3 s in O_2-saturated 0.1 M $HClO_4$ electrolyte. To obtain well-defined ORR polarization curves and the optimal MA, the Pt loadings on Pt/C, chem-Pt/flat-GC, APD-Pt/flat-GC, and APD-Pt/needles-GC were 17.9, 10.3, 2.6, and 3.1 μg_{Pt} cm^{-2}, respectively. For a fair comparison, the background current was corrected for the ORR polarization curve of Pt/C because a high surface area carbon relative to the GC was used.

Atomic-scale structures and lattice spacings for representative Pt NPs for the APD-Pt/flat-GC and APD-Pt/nanoneedles-GC were analysed using HAADF-STEM (Figure 4). Interestingly, considerable single Pt atoms as precursors for Pt NPs were observed with the APD-fabricated Pt/GC electrodes as imaged in Figure 4a & b and Figure S6. During the APD process, the highly-energetic Pt ions bombard the GC surface, which produces carbon defects of GC to bring about interaction with arriving Pt.[32] In the case of APD-Pt/nanoneedles-GC, carbon defects of GC may also have been produced during the plasma nanoneedle fabrication. The existence of considerable Pt single atoms indicates strong interactions/contacts between deposited Pt single atoms and carbon defects. Otherwise, the Pt single atoms should have spontaneously merged to NPs driven by the high kinetic energy. In addition, low-coordinated steps (Figure 4 a, c) were observed with

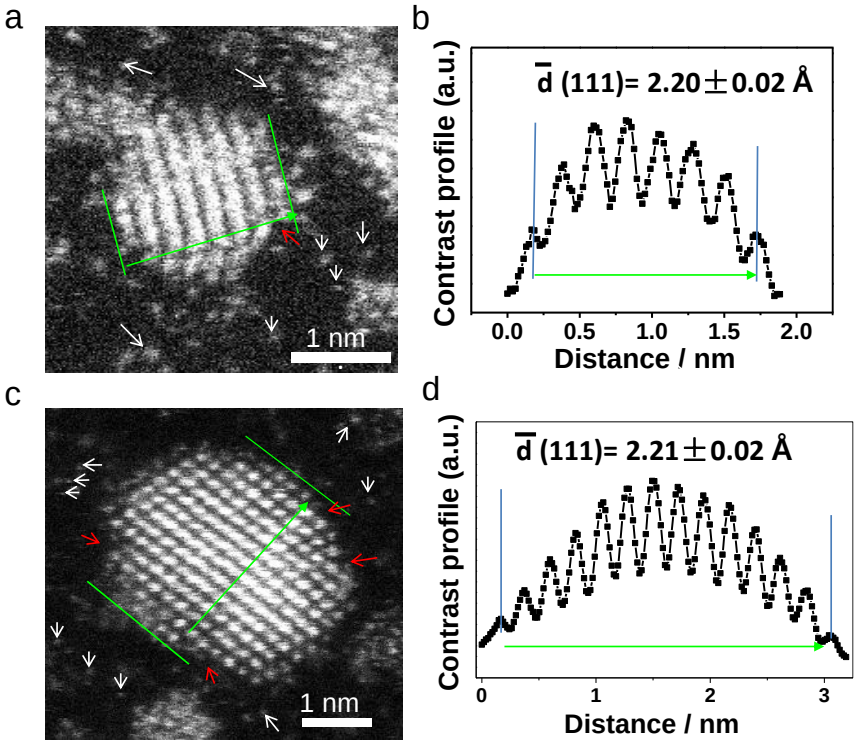

Figure 4. (a, c) Atomically-resolved HAADF-STEM images and (b, d) the corresponding lattice spacing analysis for representative Pt NPs in APD-Pt/flat-GC (a-b) and APD-Pt/nanoneedles-GC (c-d). The white arrows show single Pt atoms and red arrows indicate surface defects. The HAADF-STEM was characterized after electrochemical measurements

Pt NPs of the APD-Pt/flat-GC and APD-Pt/nanoneedles-GC, which bring about the cathodic shifts of CO_{ad} stripping peaks.

The analysis of the d(111) spacings of single Pt NPs by HAADF-STEM shows compressive strains (2.20 ±0.02 Å and 2.21±0.02 Å, respectively for APD-Pt/flat-GC (Figure 4a & b) and APD-Pt/ nanoneedles-GC (Figure 4c & d)) against 2.27 Å for the bulk, which is also caused by the strong Pt–GC contact.[10,33-35] The *in situ* EXAFS analysis at 0.4 V_{RHE} (Table S1) revealed averaged structural parameters, Pt-Pt =2.74 ±0.01 Å and coordination number (CN) of Pt-Pt bond =9.7 ±0.5 against 2.77 Å (CN(Pt-Pt) =12) for Pt bulk, which supports the compressive strain of the lattice spacing observed with the single NPs in Figure 4. The modified lattice strain and d electronic states are reported to be key issues for ORR promotion.[36-39]

Recently, Chattot et al. proposed that a structural descriptor, surface distortion (local microstrain), induces enhancement of the ORR kinetics on various $PtNi_xC$ nanostructures. Surface distortion is correlated with structural defects and/or chemical disorder, like grain boundaries, inhomogeneous alloying, and electrochemical surface destruction,[40-42] and they can be determined from wide-angle X-ray scattering (WAXS)[41] and the CO_{ad} stripping measurements.[40,42] The step defects imaged by the atom-resolved HAADF- STEM in Figure 4 and about 50–130 mV negative shifts in CO_{ad} stripping peak relative to Pt/C in Figure 3a suggest that the structural defects in APD-Pt/flat-GC and APD-Pt/nanoneedles-GC may contribute to enhancement of the ORR kinetics.

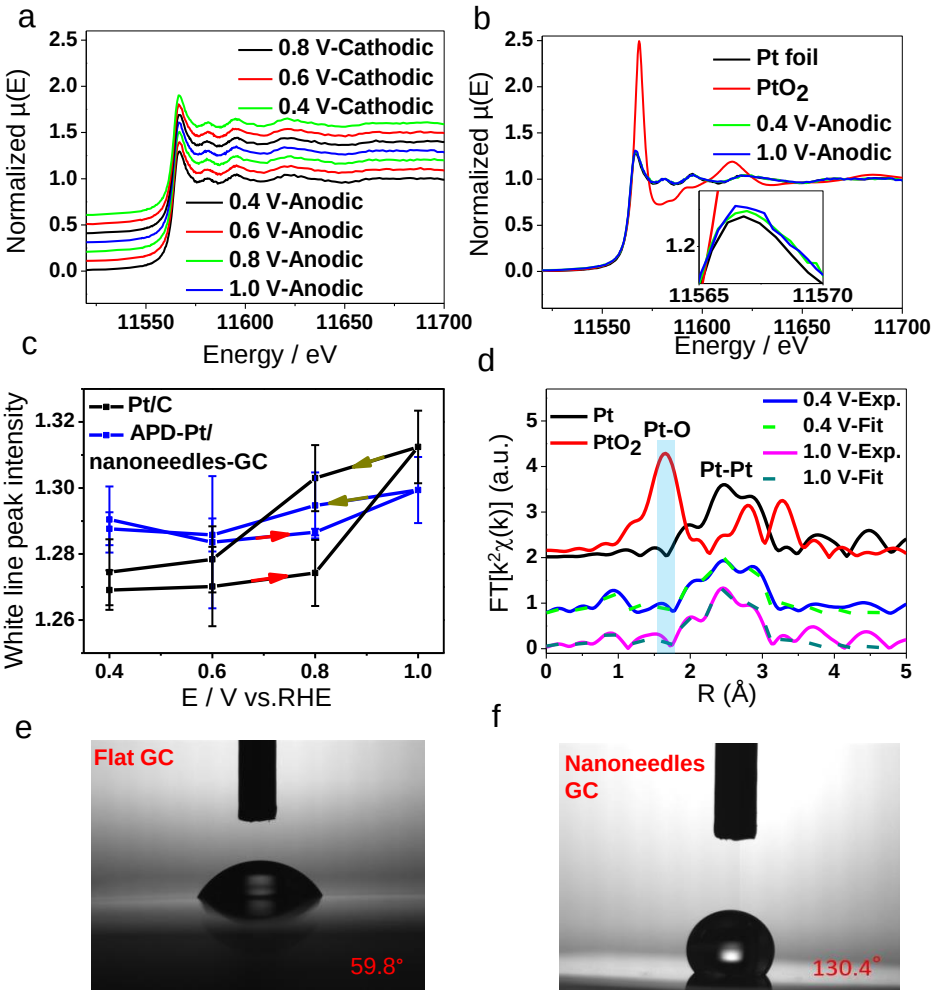

Figure 5. (a, b) *In situ* XANES spectra of APD-Pt/nanoneedles-GC recorded at anodic-scan potentials of 0.4, 0.6, 0.8, and 1.0 V_{RHE} as well as at cathodic-scan potentials of 0.8, 0.6, and 0.4 V_{RHE}. They trace dynamic change in surface oxygenated species to mimic ORR working conditions at different stages. (c) White line peak intensity changes against applied potentials for APD-Pt/nanoneedles-GC and benchmark Pt/C. (d) *In situ* k^2-weighted EXAFS Fourier-transforms for APD-Pt/nanoneedles-GC and Pt foil and PtO_2 as references. Solid lines: observed; Broken lines: fitted. (e, f) Contact angles for flat-GC and nanoneedles-GC.

To obtain *in situ* spectroscopic insight into the effects of GC-support nanoscale morphology and strong Pt–GC support contact, we measured *in situ* Pt L_3-edge XAFS spectra for the APD-Pt/nanoneedles-GC (Figure 5a–d). The applied potentials were anodically changed from 0.4 to 1.0 V_{RHE} every 0.2 V_{RHE} and then cathodically from 1.0

to 0.4 V_{RHE} to trace dynamic changes in surface oxygenated species under ORR working conditions. The white line peak intensity, which reflects Pt 5d vacancy (Pt valence), was plotted against the applied potentials (Figure 5c). At 0.4 V, a potential in the double layer, the APD-Pt/nanoneedles-GC showed the higher Pt 5d vacancy than a benchmark Pt/C. Interestingly, a suppressed increment in the white line intensity was observed with raising potentials from 0.4 to 1.0 V_{RHE}, similar to the case of Pt alloys.[43-45] The results demonstrate that the Pt 5d vacancy was tuned by the strong contact between APD-Pt and nanoneedles-GC. The subsequently decreasing potential (cathodic scan) works for the desorption of oxygenated species and recovery of metallic Pt state. Few hysteresis (even negligible hysteresis within the experimental error bars) was observed in the loop of the potential cycling (Figure 5c), which indicates the less amount of strongly adsorbed surface oxides at 1.0 V_{RHE} for the APD-Pt/nanoneedles-GC. The size of hysteresis loops approximately scales with the durability (MA loss).[18,44,45] The suppression of strong adsorption of oxygenated species in the anodic direction and the relieved cathodic dissolution due to few hysteresis loop contribute to the robust durability for the APD-Pt/nanoneedles-GC. The oxygen species adsorbed on the APD-Pt/nanoneedles-GC surface at 1.0 V_{RHE} are readily reduced below 1.0 V_{RHE}, also resulting in the higher ORR performance.[18,43-45] Fourier transformed EXAFS data for the APD-Pt/ nanoneedles-GC at both 0.4 and 1.0 V_{RHE} showed no Pt-O bonds except Pt-Pt bonds (Figure 5d and Table S1). The results on the active and durable APD-Pt/nanoneedles-GC are entirely different from those for the Pt/C, which showed the increase in the white line intensity above 0.8 V_{RHE} and the existence of Pt-O bonds in addition to Pt-Pt bonds at 1.0 V_{RHE}.[18,43-45] It is, in general, hard to detect Pt−C interface bonding due to mismatch of the lattice parameters and disordered carbon surfaces diminishing Pt−C contribution.[13] We further measured contact angles (Figure 5e & f) and the surfaces of nanoneedles-GC and flat-GC were found to be hydrophobic and hydrophilic, respectively, which confirms that the nanoneedles-structure modified the hydrophobicity/hydrophilicity of the GC surface. The contact angle data indicate that the nanoneedles-GC array may improve O_2 gas interfacial

transport and thus benefit the ORR performance of Pt NPs in 0.1 M $HClO_4$ aqueous solution through modifying hydrophobicity/hydrophilicity of the GC surface. These results on the new devised Pt/C model electrodes verify the doubly beneficial roles of plasma-fabricated nanoneedles-GC morphology and arc plasma-devised Pt NPs–nanoneedles-GC interface in the electrocatalytic ORR.

4. CONCLUSIONS

We devised new Pt/C model electrodes to distinguish and understand the beneficial roles of nanoscale fabricated carbon surface and devised Pt–carbon interface in remarkable improvements of Pt/carbon fuel cell electrodes. The doubly beneficial contribution of the nanoneedles-GC support morphology and strong Pt–GC support contact to the electrocatalytic ORR was observed with the Pt/C model electrode constituting the high energy APD-devised Pt NPs and the plasma-fabricated nanoneedles-GC. The ORR activity and durability of APD-Pt/nanoneedles-GC, APD-Pt/flat-GC, chem-Pt/flat-GC, and commercial Pt/C were compared, and the highly enhanced activity and remarkable durability of the APD-Pt/nanoneedles-GC electrode by the doubly beneficial effects of support nanoscale morphology and strong metal–support interface were evidenced by the intimate combination of controlled Pt/GC synthesis, electrochemical measurements, *in situ* XAFS and HAADF-STEM. The nanoneedles-GC support morphology at RDE in 0.1 M $HClO_4$ may improve oxygen gas transport at nanoscale through modifying the hydrophobicity/hydrophilicity of the GC surface. The strong Pt–GC interfacial interactions modify the d electronic structure of Pt NPs, resulting in the suppression of strongly adsorbed oxygenated species. The atom-resolved HAADF-STEM images and CO_{ad} stripping potentials suggest that the structural defects and compressive strain of Pt NPs induced by the strong metal-support contact in the plasma-devised electrodes may benefit the ORR activity of APD-Pt/nanoneedles-GC. These findings with the devised Pt/C model electrodes would guide how to conceive and prepare better active and durable fuel cell electrodes, metal-air batteries, and catalytic materials.

ASSOCIATED CONTENT

Supporting Information

HAADF-STEM images for APD-Pt/nanoneedles-GC and APD-Pt/flat-GC, TEM and particle size histogram, ORR polarization curves of chem-Pt/flat-GC and APD-Pt/flat-GC, and EXAFS curve-fitting results. This material is available free of charge via the Internet at http://pubs.acs.org.

AUTHOR INFORMATION

Corresponding Author

iwasawa@pc.uec.ac.jp

Author Contributions

The manuscript was written through contributions of all authors. All authors have given approval to the final version of the manuscript. All authors contributed equally.

Funding Source

Polymer Electrolyte Fuel Cell Program under New Energy and Industrial Technology Development Organization (NEDO)

Notes

The authors declare no competing financial interest.

ACKNOWLEDGMENTS

This work was supported by New Energy and Industrial Technology Development Organization (NEDO), Ministry of Economy, Trade, and Industry (METI), Japan. XAFS measurements were performed with the approval of SPring-8 subject numbers 2017A7800, 2017A7807, 2017A7808, 2017B7800, 2017B7806, 2018A7800, 2018A7806, 2018B7800, 2019A7800 and 2019B7800. We thank K. Iwahori, K. Yoneyama and M. Ousaka and H. Iwaya in Material & Advanced Research Laboratory,

Nikon Corp. for contact angle and SEM measurements, respectively. We also thank Dr. Yoshiaki Agawa in Advance Riko. Inc. for the assistance of APD experiments.

REFERENCES

(1) Guo, S. J.; Zhang, S.; Sun, S. H. Tuning Nanoparticle Catalysis for the Oxygen Reduction Reaction. *Angew. Chem. Int. Ed.* **2013,** *52*, 8526-8544.

(2) Seh, Z. W.; Kibsgaard, J.; Dickens, C. F.; Chorkendorff, I.; Nørskov, J. K.; Jaramillo, T. F. Combining theory and experiment in electrocatalysis: Insights into materials design. *Science* **2017,** *355*, eaad4998.

(3) Shao, M.; Chang, Q.; Dodelet, J.-P.; Chenitz, R. Recent Advances in Electrocatalysts for Oxygen Reduction Reaction. *Chem. Rev.* **2016,** *116*, 3594-3657.

(4) Klinkova, A.; De Luna, P.; Dinh, C.-T.; Voznyy, O.; Larin, E. M.; Kumacheva, E.; Sargent, E. H. Rational Design of Efficient Palladium Catalysts for Electroreduction of Carbon Dioxide to Formate. *ACS Catal.* **2016,** *6*, 8115-8120.

(5) Burdyny, T.; Graham, P. J.; Pang, Y.; Dinh, C.-T.; Liu, M.; Sargent, E. H.; Sinton, D. Nanomorphology-Enhanced Gas-Evolution Intensifies CO2 Reduction Electrochemistry. *ACS Sustainable Chemistry & Engineering* **2017,** *5*, 4031-4040.

(6) Liu, M.; Pang, Y.; Zhang, B.; De Luna, P.; Voznyy, O.; Xu, J.; Zheng, X.; Dinh, C. T.; Fan, F.; Cao, C.; de Arquer, F. P. G.; Safaei, T. S.; Mepham, A.; Klinkova, A.; Kumacheva, E.; Filleter, T.; Sinton, D.; Kelley, S. O.; Sargent, E. H. Enhanced electrocatalytic CO_2 reduction via field-induced reagent concentration. *Nature* **2016,** *537*, 382.

(7) Yu, S.-H.; Gao, F.-Y.; Hu, S.-J.; Zhang, X.-L.; Zheng, Y.-R.; Niu, Z.-Z.; Yang, P.-P.; Bao, R.-C.; Ma, T.; Dang, Z.; Guan, Y.; Zheng, X.-S.; Zheng, X.; Zhu, J.-F.; Gao, M.-R.; Zhang, H.-J. High-curvature transition metal chalcogenide nanostructures with profound proximity effect enable fast and selective CO2 electroreduction. *Angew. Chem. Int. Ed.*. doi:10.1002/anie.201912348.

(8) Saberi Safaei, T.; Mepham, A.; Zheng, X.; Pang, Y.; Dinh, C.-T.; Liu, M.; Sinton, D.; Kelley, S. O.; Sargent, E. H. High-Density Nanosharp Microstructures Enable Efficient CO_2 Electroreduction. *Nano Lett.* **2016,** *16,* 7224-7228.

(9) De Luna, P.; Quintero-Bermudez, R.; Dinh, C.-T.; Ross, M. B.; Bushuyev, O. S.; Todorović, P.; Regier, T.; Kelley, S. O.; Yang, P.; Sargent, E. H. Catalyst electro-redeposition controls morphology and oxidation state for selective carbon dioxide reduction. *Nature Catalysis* **2018**.

(10) Gerber, I. C.; Serp, P. A Theory/Experience Description of Support Effects in Carbon-Supported Catalysts. *Chem. Rev.* **2019**.

(11) Zhao, X.; Gunji, T.; Kaneko, T.; Takao, S.; Sakata, T.; Higashi, K.; Yoshida, Y.; Ge, J.; Liu, C.; Xing, W.; Zhu, J.; Xiao, M.; Uruga, T.; Tao, F.; Chen, Z. Evidence for interfacial geometric interactions at metal–support interfaces and their influence on the electroactivity and stability of Pt nanoparticles. *J. Mater. Chem. A* **2020,** *8,* 1368-1377.

(12) Zhao, X.; Zhu, J.; Liang, L.; Liao, J.; Liu, C.; Xing, W. Enhanced activity of Pt nano-crystals supported on a novel TiO2@ N-doped C nano-composite for methanol oxidation reaction. *J. Mater. Chem.* **2012,** *22,* 19718-19725.

(13) Kaneko, T.; Samjeské, G.; Nagamatsu, S.-i.; Higashi, K.; Sekizawa, O.; Takao, S.; Yamamoto, T.; Zhao, X.; Sakata, T.; Uruga, T.; Iwasawa, Y. Key Structural Kinetics for Carbon Effects on the Performance and Durability of Pt/Carbon Cathode Catalysts in Polymer Electrolyte Fuel Cells Characterized by In Situ Time-Resolved X-ray Absorption Fine Structure. *J. Phys. Chem. C* **2016**, *120*, 24250–24264.

(14) Ponomarev, I. I.; Zhigalina, O. M.; Skupov, K. M.; Modestov, A. D.; Basu, V. G.; Sufiyanova, A. E.; Ponomarev, I. I.; Razorenov, D. Y., Preparation and thermal treatment influence on Pt-decorated electrospun carbon nanofiber electrocatalysts. *RSC Advances* **2019,** *9,* 27406-27418.

(15) Schonvogel, D.; Hülstede, J.; Wagner, P.; Kruusenberg, I.; Tammeveski, K.; Dyck, A.; Agert, C.; Wark, M. Stability of Pt Nanoparticles on Alternative Carbon Supports for Oxygen Reduction Reaction. *J. Electrochem. Soc.* **2017,** *164*, F995-F1004.

(16) Hatakeyama, R. Nanocarbon materials fabricated using plasmas. *Rev. Mod. Plasma Phys.* **2017**, *1*, 7. doi.org/10.1007/s41614-017-0009-y

(17) Todoroki, N.; Kato, T.; Hayashi, T.; Takahashi, S.; Wadayama, T. Pt−Ni Nanoparticle-Stacking Thin Film: Highly Active Electrocatalysts for Oxygen Reduction Reaction. *ACS Catal.* **2015**, *5*, 2209−2212.

(18) Nagasawa, K.; Takao, S.; Nagamatsu, S.; Samjeské, G.; Sekizawa, O.; Kaneko, T.; Higashi, K.; Yamamoto, T.; Uruga, T.; Iwasawa, Y. Surface-Regulated Nano-SnO_2/Pt_3Co/C Cathode Catalysts for Polymer Electrolyte Fuel Cells Fabricated by a Selective Electrochemical Sn Deposition Method. *J. Am. Chem. Soc.* **2015**, *137*, 12856-12864.

(19) Uruga, T.; Tada, M.; Sekizawa, O.; Takagi, Y.; Yokoyama, T.; Iwasawa, Y. SPring-8 BL36XU: Synchrotron Radiation X-ray-Based Multi-Analytical Beamline for Polymer Electrolyte Fuel Cells under Operating Conditions. *Chem. Rec.* **2019**, *19*, 1444-1456.

(20) *XAFS Techniques for Catalysts, Nanomaterials, and Surfaces (Iwasawa, Y., Asakura, K., Tada, M., Eds.)*, Springer Nature, 2017.

(21) Ravel, B.; Newville, M. ATHENA, ARTEMIS, HEPHAESTUS: Data Analysis for X-ray Absorption Spectroscopy using IFEFFIT. *J. Synchrotron Radiat*. **2005**, *12*, 537-541.

(22) Shao, M.; Chang, Q.; Dodelet, J.-P.; Chenitz, R. Recent Advances in Electrocatalysts for Oxygen Reduction Reaction, *Chem. Rev.* **2016**, *116*, 3594-3657.

(23) Zhao, X.; Gunji, T.; Kaneko, T.; Yoshida, Y.; Takao, S.; Higashi, K.; Uruga, T.; He, W.; Liu, J.; Zou, Z. An Integrated Single-Electrode Method Reveals the Template Roles of Atomic Steps: Disturb Interfacial Water Networks and Thus Affect the Reactivity of Electrocatalysts. *J. Am. Chem. Soc.* **2019,** *141*, 8516-8526.

(24) Tian, X.; Zhao, X.; Su, Y.-Q.; Wang, L.; Wang, H.; Dang, D.; Chi, B.; Liu, H.; Hensen, E. J. M.; Lou, X. W.; Xia, B. Y. Engineering bunched Pt-Ni alloy nanocages for efficient oxygen reduction in practical fuel cells. *Science* **2019,** *366*, 850-856.

(25) Martens, I.; Chattot, R.; Rasola, M.; Blanco, M. V.; Honkimäki, V.; Bizzotto, D.; Wilkinson, D. P.; Drnec, J. Probing the Dynamics of Platinum Surface Oxides in Fuel Cell Catalyst Layers Using in Situ X-ray Diffraction. *ACS Appl. Energy Mater.* **2019,** *2*, 7772-7780.

(26) Mayrhofer, K. J. J.; Strmcnik, D.; Blizanac, B. B.; Stamenkovic, V.; Arenz, M.; Markovic, N. M. Measurement of oxygen reduction activities via the rotating disc electrode method: From Pt model surfaces to carbon-supported high surface area catalysts. *Electrochim. Acta* **2008,** *53*, 3181-3188.

(27) Garsany, Y.; Singer, I. L.; Swider-Lyons, K. E. Impact of film drying procedures on RDE characterization of Pt/VC electrocatalysts. *J. Electroanal. Chem.* **2011,** *662*, 396-406.

(28) P.I., S. S. K. Best Practices and Benchmark Activities for ORR Measurements by the Rotating Disk Electrode Technique. *http://www.hydrogen.energy.gov/pdfs/review14/fc111_kocha_2014_o.pdf* (**2014**).

(29) Meier, J. C.; Galeano, C.; Katsounaros, I.; Topalov, A. A.; Kostka, A.; Schüth, F.; Mayrhofer, K. J. J. Degradation Mechanisms of Pt/C Fuel Cell Catalysts under Simulated Start–Stop Conditions. *ACS Catal.* **2012,** *2*, 832-843.

(30) Cherevko, S.; Kulyk, N.; Mayrhofer, K. J. J. Durability of platinum-based fuel cell electrocatalysts: Dissolution of bulk and nanoscale platinum. *Nano Energy* **2016,** *29*, 275-298.

(31) Topalov, A. A.; Cherevko, S.; Zeradjanin, A. R.; Meier, J. C.; Katsounaros, I.; Mayrhofer, K. J. J. Towards a comprehensive understanding of platinum dissolution in acidic media. *Chemical Science* **2014,** *5*, 631-638.

(32) Hinokuma, S.; Misumi, S.; Yoshida, H.; Machida, M. Nanoparticle catalyst preparation using pulsed arc plasma deposition. *Catal. Sci. Technol.* **2015,** *5*, 4249-4257.

(33) Ochoa-Fernández, E.; Chen, D.; Yu, Z.; Tøtdal, B.; Rønning, M.; Holmen, A. Effect of carbon nanofiber-induced microstrain on the catalytic activity of Ni crystals. *Surf. Sci.* **2004,** *554*, L107-L112.

(34) Daio, T.; Staykov, A.; Guo, L. M.; Liu, J. F.; Tanaka, M.; Lyth, S. M.; Sasaki, K. Lattice Strain Mapping of Platinum Nanoparticles on Carbon and SnO_2 Supports. *Sci. Reports* **2015,** *5*, 13126.

(35) Gao, W.; Choi, A. S.; Zuo, J.-M. Interaction of nanometer-sized gold nanocrystals with rutile (110) surface steps revealed at atomic resolution. *Surf. Sci.* **2014,** *625*, 16-22.

(36) Stamenkovic, V.; Mun, B. S.; Mayrhofer, K. J. J.; Ross, P. N.; Markovic, N. M.; Rossmeisl, J.; Greeley, J.; Norskov, J. K. Changing the Activity of Electrocatalysts for Oxygen Reduction by Tuning the Surface Electronic Structure. *Angew. Chem. Int. Ed.* **2006**, *45*, 2897-2901.

(37) Escudero-Escribano, M.; Malacrida, P.; Hansen, M. H.; Vej-Hansen, U. G.; Velázquez-Palenzuela, A.; Tripkovic, V.; Schiøtz, J.; Rossmeisl, J.; Stephens, I. E. L.; Chorkendorff, I. Tuning the activity of Pt alloy electrocatalysts by means of the lanthanide contraction. *Science* **2016,** *352*, 73-76.

(38) Hammer, B.; J.K.Nørskov, J. K. Theoretical surface science and catalysis—calculations and concepts. *Adv. Catal.* **2000**, *45*, 71-129.

(39) Strasser, P.; Koh, S.; Anniyev, T.; Greeley, J.; More, K.; Yu, C.; Liu, Z.; Kaya, S.; Nordlund, D.; Ogasawara, H.; Toney, M. F.; Nilsson, A. Lattice-strain control of the activity in dealloyed core–shell fuel cell catalysts. *Nature Chem.* **2010**, *2*, 454-460.

(40) Chattot, R.; Asset, T.; Bordet, P.; Drnec, J.; Dubau, L.; Maillard, F. Beyond Strain and Ligand Effects: Microstrain-Induced Enhancement of the Oxygen Reduction Reaction Kinetics on Various PtNi/C Nanostructures. *ACS Catal.* **2017,** *7*, 398-408.

(41) Chattot, R.; Le Bacq, O.; Beermann, V.; Kühl, S.; Herranz, J.; Henning, S.; Kühn, L.; Asset, T.; Guétaz, L.; Renou, G.; Drnec, J.; Bordet, P.; Pasturel, A.; Eychmüller, A.; Schmidt, T. J.; Strasser, P.; Dubau, L.; Maillard, F. Surface distortion as a unifying concept and descriptor in oxygen reduction reaction electrocatalysis. *Nature Mater.* **2018,** *17*, 827-833.

(42) Chattot, R.; Martens, I.; Scohy, M.; Herranz, J.; Drnec, J.; Maillard, F.; Dubau, L. Disclosing Pt-Bimetallic Alloy Nanoparticle Surface Lattice Distortion with Electrochemical Probes. *ACS Energy Letters* **2020,** *5*, 162-169.

(43) Mukerjee, S.; Srinivasan, S.; Soriaga, M. P.; McBreen, J. Role of Structural and Electronic Properties of Pt and Pt Alloys on Electrocatalysis of Oxygen Reduction: An In Situ XANES and EXAFS Investigation. *J. Electrochem. Soc.* **1995,** *142*, 1409-1422.

(44) Zhao, X.; Takao, S.; Higashi, K.; Kaneko, T.; Samjeskè, G.; Sekizawa, O.; Sakata, T.; Yoshida, Y.; Uruga, T.; Iwasawa, Y. Simultaneous Improvements in Performance and Durability of an Octahedral PtNix/C Electrocatalyst for Next-Generation Fuel Cells by Continuous, Compressive, and Concave Pt Skin Layers. *ACS Catal.* **2017,** *7*, 4642-4654.

(45) Zhao, X.; Takao, S.; Kaneko, T.; Iwasawa, Y. Key Factors for Simultaneous Improvements of Performance and Durability of Core-Shell Pt3Ni/Carbon Electrocatalysts Toward Superior Polymer Electrolyte Fuel Cell. *Chem. Record* **2019,** *19*, 1337-1353.

TOC

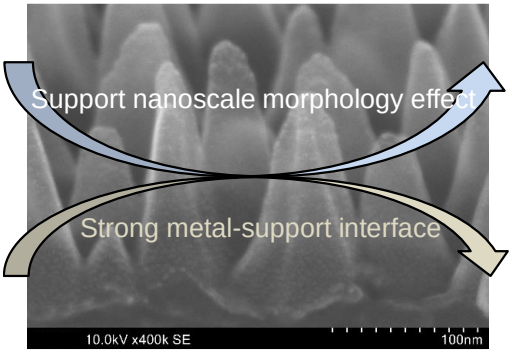
Support nanoscale morphology effect
Strong metal-support interface
10.0kV x400k SE
100nm